J. Fluid Mech. (2002), *vol.* 469, *pp.* 1–12.
DOI: 10.1017/S002211200200174X Printed in the United Kingdom

High-Rayleigh-number convection of pressurized gases in a horizontal enclosure

By A. S. FLEISCHER[1]† AND R. J. GOLDSTEIN[2]

[1]Department of Mechanical Engineering, Villanova University, 800 Lancaster Ave, Villanova, PA 19085, USA
amy.fleischer@villanova.edu

[2]Heat Transfer Laboratory, Mechanical Engineering Department, University of Minnesota, Minneapolis, MN 55455, USA
rjg@me.umn.edu

(Received 13 July 2001 and in revised form 28 May 2002)

High-pressure gases are used to study high-Rayleigh-number Rayleigh–Bénard convection in cylindrical horizontal enclosures. The Nusselt–Rayleigh heat transfer relationship is investigated for $1 \times 10^9 < Ra < 1.7 \times 10^{12}$. Schlieren video images of the flow field are recorded through optical viewports in the pressure vessel. The data set is well correlated by $Nu = 0.071Ra^{0.328}$. The schlieren results confirm the existence of a large-scale flow that periodically interrupts the ascending and descending plumes. The intensity of both the plumes and the large-scale flow increases with Rayleigh number.

1. Introduction

Natural convection is present in many situations. An oft-studied example is Rayleigh–Bénard flow in a horizontal enclosure, with the upper and lower plates maintained isothermal. When the Rayleigh number (Ra) of the system exceeds a critical level, flow begins in the enclosure. The low-density fluid near the warm bottom plate rises toward the upper plate. Near the upper plate, the fluid cools, increasing its density until it sinks to the lower plate where the cycle begins again, establishing a flow pattern. This flow pattern takes many forms, including hexagons, rolls or plumes, depending on Ra.

When $Ra > 10^7$, the flow typically takes the form of ascending and descending plumes, or thermals. Howard (1966) postulates that high-Rayleigh-number convection consists of the build-up of a conduction boundary layer, followed by a short interval during which the warm, low-density boundary layer is swept up in a rising thermal.

Scaling arguments for Rayleigh–Bénard natural convection when $Ra > 10^7$ reveal that Nusselt numbers $Nu \sim Ra^{1/3}$ (Jakob 1946; Malkus 1954; Kraichnan 1962; Howard 1966). Several heat transfer experiments verify this $Ra^{1/3}$ relationship for rates as high as $Ra = 10^{12}$, including Goldstein & Tokuda (1980) and Goldstein, Chiang & See (1990).

Many other experiments though, show results with a power-law relationship of $Nu \sim Ra^{2/7}$. The first to present such results, Heslot, Castaing & Libchaber (1987) find $Nu \sim Ra^{2/7}$ for $Ra > 10^7$. Wu & Libchaber (1992) study convection in low-temperature helium gas at 4 K, and find 2/7 scaling for $Ra > 10^8$. Belmonte, Tilgner & Libchaber

† Author to whom correspondence should be addressed.

Date	Authors	Ra	Pr	Fluid	Aspect ratio	Nu–Ra
1980	Goldstein & Tokuda	10^8–10^{11}	6.5	Water	0.6–4.5	$Nu = 0.0556Ra^{1/3}$
1987	Heslot *et al.*	10^7–10^{11}	0.65–1	Cryogenic helium	1	$Nu = 1 + 0.2Ra^{0.282}$
1989	Castaing *et al.*	10^7–10^{12}	0.6–1.5	Cryogenic helium	0.5–1	$Nu = 0.23Ra^{0.282}$
1990	Goldstein *et al.*	10^9–10^{12}	2750	Electrochemical	varies	$Sh = 0.0659Ra^{1/3}$
1992	Wu & Libchaber	10^9–10^{10}	0.64–1	Cryogenic helium	6.7	$Nu = 0.146Ra^{2/7}$
		10^9–10^{12}			0.5	$Nu = 0.17Ra^{0.29}$
		10^9–10^{12}			1.0	$Nu = 0.17Ra^{0.285}$
1994	Belmonte *et al.*	10^5–10^{11}	0.7	Helium, nitrogen, SF_6	1	$Nu = 0.22Ra^{0.285}$
1997	Liu & Ecke	10^5–10^8	3–7	Water	0.78	$Nu = 0.164Ra^{0.286}$
1999	Ashkenazi & Steinberg	10^9–10^{14}	1–93	SF_6	1.38	$Nu = 0.22Ra^{0.3}Pr^{-0.2}$
2000	Xu *et al.*	10^5–10^{10}	4.0	Acetone	0.5–12.8	$Nu = A\ Ra^b$ where $0.277 < b < 0.300$, increasing with Ra
2000	Niemela *et al.*	10^6–10^{17}	0.7–12	Cryogenic helium	0.5	$Nu = 0.124Ra^{0.309}$

TABLE 1. Recent high-Rayleigh-number experiments.

(1994) find that for $Ra > 2 \times 10^7$, the thermal boundary layer scales with $Ra^{-2/7}$. Their schlieren visualization results for $3 \times 10^8 < Ra < 7 \times 10^{10}$ show the presence of a large-scale circulation. Chu & Goldstein (1973) observe a large-scale flow in an interferometric study. Liu & Ecke (1997) and Xu, Bajaj & Ahlers (2000) also present results consistent with a $2/7$ power law.

Most recently, a few researchers show results consistent with the power-law relationship $Nu \sim Ra^{0.31}$. In a significant paper, (Niemela, Skrbek & Donnelly 2000) a correlation of $Nu = 0.124Ra^{0.309}$ is reported over the range $10^6 < Ra < 10^{17}$. This is an extremely well-controlled experiment in cryogenic helium. In fact, the authors correct the data of Wu & Libchaber (1992) with the most up-to-date gas property data for cryogenic helium. The corrected data correlate with the equation $Nu = 0.146Ra^{0.299}$, rather than with $Nu = 0.146Ra^{2/7}$. However, the uncertainty values indicate that neither a $2/7$ nor a 0.31 scaling relationship can be ruled out. The results of Ashkenazi & Steinberg (1999) in SF_6 near the critical point show that $Nu = 0.22Ra^{0.3}Pr^{-0.2}$, where Pr is the Prandtl number.

Table 1 lists a summary of recent high-Rayleigh-number heat transfer experiments.

The present experiment investigates the relationship between Nusselt number and Rayleigh number for $10^9 < Ra < 10^{12}$ in pressurized nitrogen and argon. Of interest is whether the Nu–Ra^n relationship scales with the classical $Ra^{1/3}$, with $Ra^{2/7}$, or with $Ra^{0.31}$. Additionally, the flow pattern is identified through schlieren flow visualization. Of interest is how the behaviour of the plumes and the large-scale flow change with increasing Rayleigh number. In this experiment, the conventional definition of Rayleigh number for Rayleigh–Bénard convection is used, $Ra = g\beta(\Delta T)L^3/(\nu\alpha)$, where g is the gravitional constant, β is the coefficient of thermal expansion, ΔT is the temperature difference between the top and bottom plates, L is the distance between the plates, ν is Kinematic viscosity and α is thermal diffusivity.

2. Experimental configuration

The choice of operating fluid plays a significant role in determining the operating Rayleigh number range. The Rayleigh number is maximized by selecting gases with low thermal conductivity, low viscosity and large density. Other considerations are the existence of accurate thermophysical property data for the gas over the range of desired operating conditions; the overall safety of the gas including toxicity, flammability and corrosivity; and the availability and cost of the gas.

Several different gases are considered for this experiment, including nitrogen, argon, krypton, xenon and sulphur hexafluoride (SF_6). Krypton and xenon have high densities and inherent safety. Both are appealing choices; however, the relative scarceness of these gases, and the volume of gas required means that the cost of completing this experiment with either gas would be prohibitive. Concerns about operating too close to the critical point and introducing non-Boussinesq effects eliminates SF_6 as a viable choice in this situation.

Nitrogen is selected as the primary operating fluid due to its safety, abundant inexpensive supply, and availability of extensive high-pressure property data. The use of nitrogen at pressures up to 80 bar results in a maximum Rayleigh number of about 1×10^{12} when $L = 0.45$ m. The use of argon does not result in a significant increase in Rayleigh number over that for nitrogen; however, some test runs are made with argon to ensure the results are not operating-fluid specific, and to extend the operating range slightly to 1.7×10^{12}.

The convection cell consists of cylindrical lower and upper aluminium plates separated by a clear acrylic cylinder (see figure 1). The bottom plate is 12.7 mm thick and 457.2 mm in diameter. The rear of the plate has two grooves that separate it into three concentric rings. An independently controlled etched foil Kapton heater is applied to each ring, allowing individual adjustment for heat losses.

The sidewall is clear acrylic piping with an inner diameter of 444.5 mm and 6.35 mm wall thickness (457.2 mm outer diameter, matching that of the bottom plate). Several different heights are used (150 mm, 350 mm and 450 mm) depending on the desired Rayleigh number. The aspect ratio (L/D) is 2.96, 1.27 or 0.99 depending on sidewall height.

A calcium silicate insulating guard plate and a copper backing plate are located immediately below the bottom plate. An etched foil heater on the backing plate maintains the guard plate at the same temperature as the bottom plate, reducing heat loss from the bottom plate.

The top plate is designed with an integral spiral three-dimensional heat exchanger allowing water from a constant-temperature bath to circulate. The cool water removes the heat added at the bottom surface and typically maintains the top plate isothermal within 0.1 °C, verified by the measurement of temperature at various locations in the top plate using calibrated thermocouples from the same spool of wire.

The assembled convection cell rests on three aluminium support legs, which are thermally isolated from the copper backing plate by ceramic balls. The outside of the convection cell is insulated with glass wool.

The convection cell is contained in a large pressure vessel designed to withstand a maximum operating pressure of 92 bar (1340 p.s.i.). The vessel is fabricated from 22.2 mm thick rolled steel plate. The vessel outer diameter is 610 mm, the inner diameter is 565 mm and it has an elliptical bottom head and a flanged top.

Sight glasses are provided on either side of the vessel, 180° apart to allow schlieren visualization of the flow inside the convection cell. The sight glasses are a laminate of two pieces of the tempered Pyrex, each 32 mm thick, and each designed to withstand

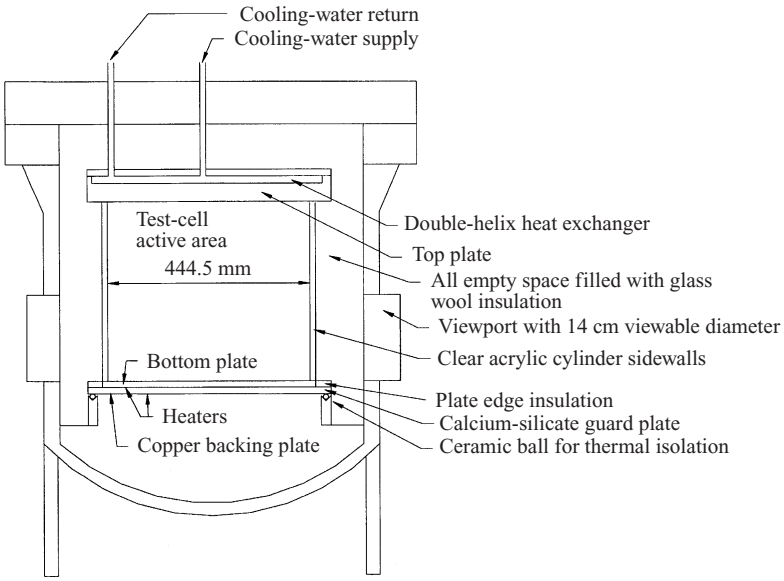

FIGURE 1. Test cell schematic.

the entire pressure alone. The tempered Pyrex is heat treated to improve its strength and thermal shock resistance. The viewable diameter is 140 mm.

3. Instrumentation and test procedure

The temperatures of the top, bottom and guard plates are monitored with calibrated Type T thermocouples. Thermocouples are embedded at up to five locations in each plate. The ambient temperature is also monitored.

Vessel pressure is measured with a pressure transducer. The voltages across the thermocouples, the pressure transducers and the etched foil heaters are monitored with a Keithley 196 digital multimeter, used with a two-card 20-channel Keithley scanner. Power to the etched foil heaters is provided by a Hewlett Packard power supply system. The system consists of a mainframe, model HP6600 MPS, with seven independently controlled power supply modules. The power supply mainframe directly monitors the current in each circuit and supplies that information to the data acquisition program.

The equipment for the schlieren flow visualization includes two optical quality mirrors, a 12 V, 65 W halogen lamp and a Panasonic WVBD400 video camera. The lamp is housed in a wooden box with a slit opening that approximates a point source. The lamp is placed at the focal point of the first mirror. The diverging light from this source becomes a beam of parallel light when reflected off the mirror. This parallel beam of light passes through the optical viewports and across the test cell where gradients in the refractive index of nitrogen refract the light beam. The refracted light beam passes out of the vessel and reflects off the second mirror. The beam of light converges to a point and a razor blade is placed at the convergence location. A camera placed just past the convergence point captures the schlieren image.

Each test run takes approximately 4–8 hours to complete. Depending on the conditions, it takes from two to six hours to come to a steady-state situation, and

then the steady-state data is recorded for several hours. A test run is initiated by setting the proper voltage to the etched foil heaters and turning on the water circulation pump. The cool water circulation lowers the top-plate temperature as the heaters raise the bottom-plate temperature until the steady-state conditions for the test are achieved.

The data acquisition program records the top and bottom plate temperatures, heater voltages, heater currents and ambient temperatures during the test run. Data are recorded every two minutes.

4. Data reduction

The Nusselt number is calculated using the net heat flux into the test cell, which is the net power to the bottom-plate heaters, carefully adjusted for losses to the guard plate, losses due to convection from the edge of the bottom plate, losses due to convection and conduction from the sidewalls, and losses due to radiation (total losses are typically on the order of 2–6%):

$$h_{testcell} = \frac{Q_{net}}{(T_{bottomplate} - T_{topplate})\pi r_{testcell}^2}, \tag{1}$$

$$Nu = \frac{h_{testcell} L}{k_{testfluid}}, \tag{2}$$

where L is the distance between the plates.

The convection losses through the test-cell sidewall are adjusted to account for the fact that glass wool insulation does not cover the viewports, leading to increased losses in that section of the sidewall. The heat transfer coefficient in the test cell is found by iteration with the final result. The heat transfer coefficient along the vessel exterior is calculated from empirical correlations for natural convection along a vertical wall (Raithby & Hollands 1985).

The Rayleigh number is calculated from the properties of the test fluid at the operating conditions, and the temperature difference between the plates.

5. Results and discussion

5.1. *Nusselt–Rayleigh relationship*

Heat transfer data are obtained for 35 data points in the range $1 \times 10^9 < Ra < 1.7 \times 10^{12}$. The Prandtl number varies by 7.5% over the operating range, from 0.690 to 0.742. The complete set of data is presented in table 2. An uncertainty analysis using the method of propagation of errors shows that the errors in the calculated Nusselt and Rayleigh numbers are small. The uncertainty in the Rayleigh number is $\pm 2\%$, and the uncertainty in the Nusselt number is $\pm 5\%$.

The best fit to the entire data set is given by the equation $Nu = 0.0714 Ra^{0.327 \pm 0.014}$. The complete data set is shown overlaid with the best fit in figure 2. The experimental uncertainty on the best fit (0.327 ± 0.014) means that neither the classical $1/3$ data fit, nor the 0.31 data fit promoted by Niemela *et al.* (2000) may be completely ruled out for this data.

An examination of each of these fits is given in figures 3 and 4. Figure 3 shows the scatter in the data when fit with the relationship $Nu \sim Ra^{1/3}$. The data scatter evenly around the mean value of 0.0616, and are contained within $\pm 4\%$ error bars

Ra	Nu	Pr	Cylinder height (m)	Aspect ratio	Press (bar)	Operating fluid	dT (K)
1.01×10^9	66.3	0.733	0.15	2.96	19.7	N_2	6.8
1.26×10^9	69.8	0.731	0.15	2.96	18.7	N_2	9.8
2.31×10^9	82.8	0.740	0.15	2.96	29.8	N_2	6.8
2.41×10^9	83.6	0.740	0.15	2.96	29.9	N_2	7.0
2.75×10^9	84.2	0.742	0.15	2.96	29.6	N_2	8.3
4.99×10^9	103.5	0.742	0.15	2.96	41.2	N_2	7.7
5.05×10^9	101.7	0.742	0.15	2.96	43.3	N_2	7.0
5.62×10^9	108.9	0.742	0.15	2.96	46.5	N_2	6.7
1.05×10^{10}	134.0	0.740	0.15	2.96	46.2	N_2	13.7
1.32×10^{10}	144.1	0.738	0.15	2.96	56.6	N_2	11.6
1.84×10^{10}	162.9	0.735	0.15	2.96	68.8	N_2	11.2
1.94×10^{10}	166.2	0.729	0.15	2.96	75.6	N_2	10.2
3.37×10^{10}	202.4	0.729	0.35	1.27	17.9	N_2	25.8
4.54×10^{10}	222.2	0.732	0.35	1.27	21.1	N_2	24.8
6.74×10^{10}	247.5	0.735	0.35	1.27	26.4	N_2	23.3
8.72×10^{10}	278.6	0.737	0.35	1.27	31.4	N_2	20.8
1.53×10^{11}	322.0	0.738	0.35	1.27	43.3	N_2	18.9
2.33×10^{11}	369.4	0.736	0.35	1.27	57.9	N_2	16.0
1.76×10^{11}	347.5	0.736	0.45	0.99	28.9	N_2	23.4
2.71×10^{11}	401.8	0.738	0.45	0.99	37.4	N_2	21.2
4.12×10^{11}	464.6	0.739	0.45	0.99	49.4	N_2	18.4
4.86×10^{11}	472.0	0.738	0.45	0.99	59.2	N_2	15.9
5.03×10^{11}	472.5	0.732	0.45	0.99	58.9	N_2	16.4
6.95×10^{11}	527.7	0.723	0.45	0.99	74.9	N_2	14.6
8.75×10^{11}	580.8	0.714	0.45	0.99	78.7	N_2	17.4
1.02×10^{12}	600.7	0.710	0.45	0.99	78	N_2	21.2
2.22×10^9	81.4	0.692	0.15	2.96	27.3	Ar	6.6
2.33×10^9	84.9	0.692	0.15	2.96	27.2	Ar	7.0
3.82×10^9	99.5	0.691	0.15	2.96	27.3	Ar	12.1
6.20×10^9	114.9	0.690	0.15	2.96	28.2	Ar	20.5
7.37×10^{11}	559.7	0.713	0.45	0.99	58.6	Ar	19.3
7.49×10^{11}	558.9	0.713	0.45	0.99	57.6	Ar	20.1
1.19×10^{12}	652.7	0.725	0.45	0.99	77.3	Ar	16.9
1.45×10^{12}	677.0	0.724	0.45	0.99	76.5	Ar	22.1
1.68×10^{12}	716.4	0.724	0.45	0.99	77.6	Ar	25.6

TABLE 2. Complete data set.

for four decades of Rayleigh number, $2 \times 10^9 < Ra < 2 \times 10^{12}$. Thus, the data are well-approximated by the 1/3 fit $Nu = 0.0616Ra^{1/3}$.

Figure 4 shows the scatter in the data for a $Nu \sim Ra^{0.31}$ fit to the complete data set. Unlike the data in figure 3, the data in figure 4 do not scatter evenly around the mean value of 0.109. Instead, they show a distinct trend upwards. For $Ra < 2 \times 10^{10}$, the data points all remain below the mean value, and for $Ra > 2 \times 10^{10}$ the data points all remain above the mean value. Thus, while the data can be approximated with a fit of $Nu = 0.109Ra^{0.31}$, the fit is not as good as the 1/3 fit to the data.

Both the 1/3 fit and the 0.31 fit to the complete data set are shown in figure 5. As is expected from the results of figures 3 and 4, the 1/3 fit better approximates the data set. The 0.31 fit remains slightly above the data for $Ra < 2 \times 10^{10}$ and falls below the data for $Ra > 2 \times 10^{10}$.

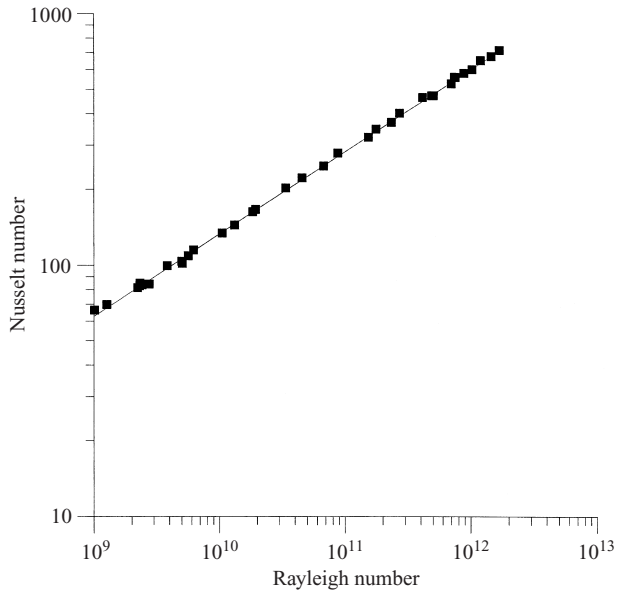

FIGURE 2. Best fit to the complete data set, $Nu = 0.0714Ra^{0.329}$.

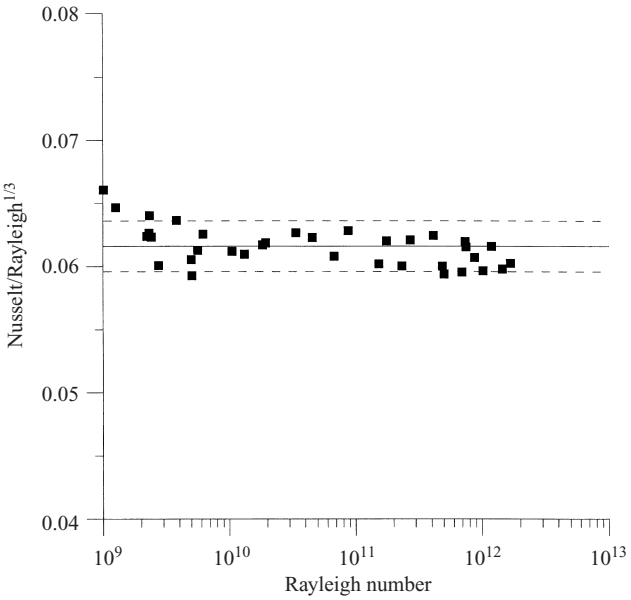

FIGURE 3. Examination of the Nu–$Ra^{1/3}$ fit to the complete data set (bounded by $\pm 4\%$ lines).

The fits to the complete data set may be interpreted as verifying the existence of a $Nu \sim Ra^{1/3}$ region, as previously found by Goldstein & Tokuda (1980) and Goldstein *et al.* (1990). However, arguments may be made that within experimental error, the data can reflect a $Nu \sim Ra^{0.31}$ scaling as previously found by Niemela *et al.* (2000). No evidence supporting the existence of a $Ra^{2/7}$ regime, as previously found by Heslot *et al.* (1987), Wu & Libchaber (1992), Belmonte *et al.* (1994), Liu & Ecke (1997) and Xu *et al.* (2000), is found in this experiment.

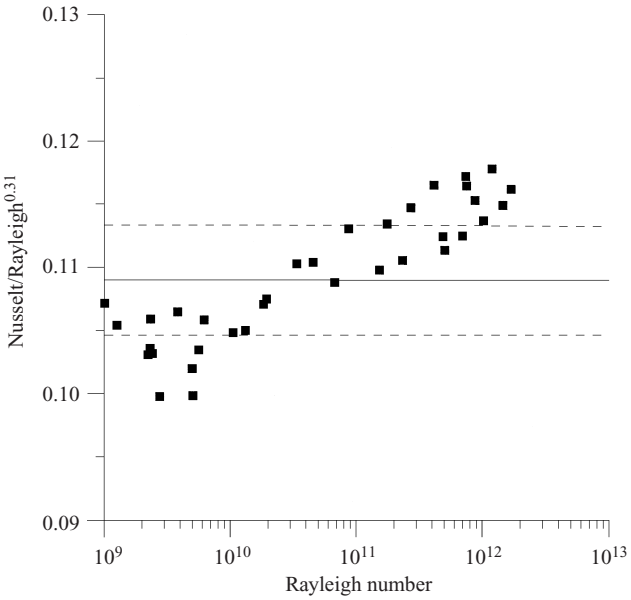

FIGURE 4. Examination of the Nu–$Ra^{0.31}$ fit to the complete data set (bounded by $\pm 4\%$ lines).

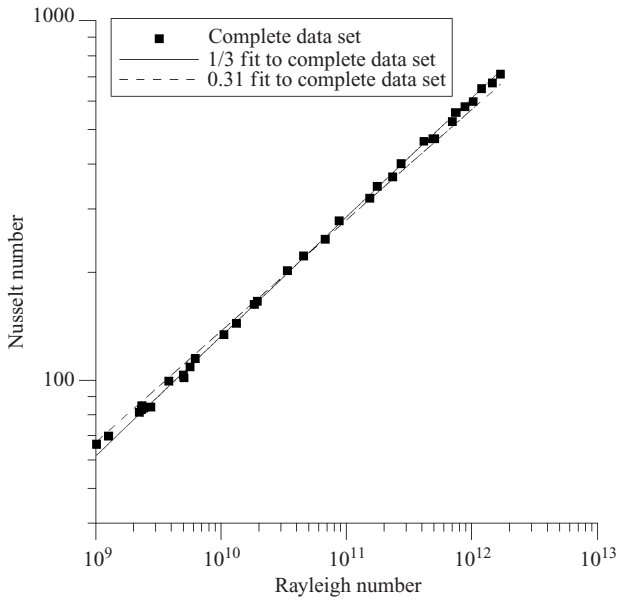

FIGURE 5. Comparison of 1/3 and 0.31 fit to the complete data set.

5.2. *Aspect ratio effects*

The highest Rayleigh numbers are reached by increasing both the operating pressure and the test cell height, L, while maintaining the diameter, D, constant. The cubic dependence of Rayleigh number on the distance between the plates causes the achievable Rayleigh range to increase with each new test cell height. As the change in test cell height changes the aspect ratio of the test cell, it is difficult to isolate the effects of aspect ratio from the effects of increasing Rayleigh number, as

Aspect ratio	Rayleigh range	Operating fluid	# data points	Best fit equation
2.96	1×10^9–1.94×10^{10}	N_2	12	$Nu = 0.0956Ra^{0.314}$
2.96	2.22×10^9–6.2×10^9	Ar	4	$Nu = 0.0736Ra^{0.326}$
1.27	3.37×10^{10}–2.33×10^{11}	N_2	6	$Nu = 0.1072Ra^{0.311}$
0.99	1.76×10^{11}–1.02×10^{12}	N_2	8	$Nu = 0.117Ra^{0.309}$
0.99	7.37×10^{11}–1.68×10^{12}	Ar	5	$Nu = 0.1577Ra^{0.299}$
All data	1×10^9–1.68×10^{12}	All data	35	$Nu = 0.0714Ra^{0.3273}$

TABLE 3. Best-fit equations for each aspect ratio.

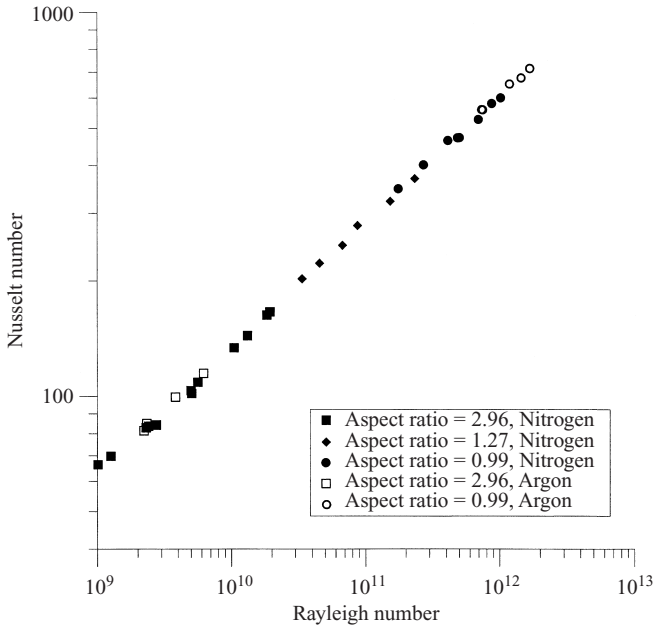

FIGURE 6. Complete data set identified by aspect ratio and operating fluid.

the two are intimately linked in this experiment. Figure 6 shows how the Rayleigh number range increases for each reduction in aspect ratio. As seen in figure 6 and table 3, several of the aspect ratios have a limited number of data points. More data need to be taken at each aspect ratio to confirm any aspect ratio effects; however the limited results will be discussed here in the general context of comparison to other aspect ratio studies.

A power-law best fit to the data for each aspect ratio shows a general trend of decreasing exponent with increasing Rayleigh number (see table 3). This can most likely be attributed to the increase in Rayleigh range for each aspect ratio. As Rayleigh increases for each aspect ratio, the data approach the $Nu \sim Ra^{0.31}$ relationship promoted by Niemela *et al.* (2000). These results show that a 0.31 relationship will fit the data well in the range $3 \times 10^{10} < Ra < 1 \times 10^{12}$. Above 1×10^{12} the data are best fit by a $Nu \sim Ra^{0.299}$ relationship, similiar to the results of Ashkenazi & Steinberg (1999) for pressurized SF_6 for Ra up to 5×10^{12}.

These data also show that as the aspect ratio decreases and the Rayleigh number increases, the front multiplier of the $Nu = ARa^n$ relationship increases. A similiar

trend is observed in the aspect ratio experiments of Xu *et al.* (2000), who studied Rayleigh–Bénard convection for aspect ratios ranging from 0.5 to 12.8. They collected data over the same Rayleigh range for different aspect ratios, thus isolating the aspect ratio effect and clearly showing a slight increase in Nu as aspect ratio decreases. Their results show that A increases as aspect ratio decreases over the same range of Rayleigh number. In this experiment's pressurized nitrogen data, the front multiplier increases from $A = 0.0956$ when the aspect ratio is 2.96, to $A = 0.1072$ when aspect ratio is 1.27, and finally to $A = 0.117$ when aspect ratio is 0.99. This reflects a 22% increase in A as the aspect ratio decreases from 3 to 1.

6. Flow visualization

Schlieren visualization for twelve Rayleigh numbers between 3.37×10^{10} and 1.19×10^{12} confirms the existence of both ascending and descending plumes, as well as a large-scale circulation which takes the form of one large roll cell with a horizontally orientated axis. The large-scale flow traverses along the top and bottom plates, ascending and descending along the sidewalls of the test cell, while the bulk of the cell remains homogenous at lower Rayleigh numbers, interrupted only by the motion of the plumes.

The visualization of the flow at $Ra = 3.37 \times 10^{10}$ and 4.54×10^{10} shows that plumes are emitted from multiple locations scattered uniformly and randomly across both the top and bottom plates. These plumes move vertically across the central bulk region of the test cell without being disrupted to any extent by the large-scale circulation roll cell along the plates. Although the bulk of the test cell remains primarily homogenous, rare horizontal bursts do occur in the central region. These bursts of horizontal flow are characterized by a sudden horizontal fluid motion in the cell, as though a sudden wind gust has blown the flow sideways. The bursts, which occur equally in each direction, tend to force the vertically moving plumes into swirls and eddies.

As Ra increases to 9×10^{10}, the circulation of the large-scale roll cell increases in both velocity and intensity. The vertical plumes continue to be able break through the intense horizontal motion of the large-scale roll cell along the upper and lower plates and traverse the central section unimpeded. The occasional horizontal burst in the central region disrupts the vertical motion of the plumes as before.

For $Ra > 10^{11}$, the height of the test cell precludes schlieren imaging of the boundary layer, because the increased height requirement necessitates that the top and bottom plates be located above and below the vessel viewports. The interaction of the plumes and large-scale flow in the central region can still be observed.

The visualization of the flow in the bulk central region of the test cell at $Ra = 1.76 \times 10^{11}$ and 2.71×10^{11} reveals that horizontal bursts are now coming more regularly in this region; they come randomly from each direction and interrupt the vertical motion of the plumes. These bursts of horizontal flow sweep the plumes horizontally, but a new plume will be initiated from the original site once the horizontal bursts weaken and dissipate.

As the Rayleigh number increases to 4×10^{11}, the horizontal bursts of flow in the bulk central region of the cell continue to intensify. They now come more steadily, from both directions, repeatedly forcing the vertically moving plumes into violent swirls and eddies. The upper edge of the large-scale single roll cell now descends through the central bulk region at approximately 45°, rather than continuing its motion across the boundary of the upper plate. The motion of the roll cell is now often disrupted by the violent bursts of horizontal flow.

The highest Rayleigh numbers studied (8.75×10^{11}, 1.02×10^{12}, 1.19×10^{12}) exhibit an extremely intense flow pattern. Continual bursts of horizontal flow in the central region create an intense continuous swirling motion throughout the bulk of the test cell. The large-scale roll-cell motion continues to persist, with the roll cell traversing the bottom plate, rising vertically along one side of the test cell and descending at approximately 45° through the bulk central region of the cell.

7. Conclusions

Convection in high-pressure gases yields a simple relationship between Nusselt number and Rayleigh number for $10^9 < Ra < 10^{12}$. The best fit to the data set is $Nu = 0.0714Ra^{0.327 \pm 0.014}$, while the data set is also well-correlated by $Nu = 0.0616Ra^{1/3}$. Arguments may be made to support $Nu = 0.109Ra^{0.31}$; however the fit is not as good as that for the 1/3 correlation. The results rule out any prediction of a 2/7 power-law relationship.

As the Rayleigh number increases, and aspect ratio decreases, the exponent on the power-law fit decreases. A 0.31 power-law relationship will fit the data well when restricted to $3 \times 10^{10} < Ra < 1 \times 10^{12}$. Above 1×10^{12} the data is best fit by a Nu–$Ra^{0.299}$ relationship.

As the aspect ratio decreases and the Rayleigh number increases, the front multiplier of the $Nu = ARa^n$ relationship increases. For the nitrogen experiments, the power-law multiplier A increases by 22% as the aspect ratio decreases from 3 to 1.

The schlieren flow visualization confirms the existence of both vertical plumes and a single large-scale roll cell in the test cell. The intensity and velocity of both the plumes and the roll cell increase with *Ra*. Periodic bursts of horizontal flow disrupt the flow pattern in the central bulk region of the test cell, forcing the vertically moving plumes into swirls and eddies. The horizontal flow bursts become steadier as *Ra* increases. As *Ra* continues to increase, the large-scale roll cell becomes non-symmetrical as it traverses the bottom plate in a horizontal motion, rises along one side of the test cell and then sinks at approximately 45° back to the bottom plate. For $Ra > 10^{12}$, the flow in the central region of the test cell is characterized by a violently swirling motion.

This material is based upon work completed while A. S. Fleischer was supported under a National Science Foundation Graduate Research Fellowship. Support by the Graduate School of the University of Minnesota is gratefully acknowledged.

REFERENCES

Ashkenazi, S. & Steinberg, V. 1999 High Rayleigh number turbulent convection in a gas near the gas-liquid critical point. *Phys. Rev. Lett.* **83**, 3641–3644.

Belmonte, A., Tilgner, A. & Libchaber, A. 1994 Temperature and velocity boundary layers in turbulent convection. *Phys. Rev.* E **50**, 269–270.

Castaing, B., Gunaratne, G., Heslut, F. *et al.* 1989 Scaling of hard thermal turbulence in Rayleigh–Bénard convection. *J. Fluid Mech.* **204**, 1–30.

Chu, T. Y. & Goldstein, R. J. 1973 Turbulent convection in a horizontal layer of water. *J. Fluid Mech.* **60**, 141–159.

Goldstein, R. J., Chiang, H. D. & See, D. L. 1990 High Rayleigh number convection in a horizontal enclosure. *J. Fluid Mech.* **213**, 111–126.

Goldstein, R. J. & Tokuda, S. 1980 Heat transfer by thermal convection at high Rayleigh numbers. *Intl J. Heat Mass Transfer* **23**, 738–740.

Heslot, F., Castaing, B. & Libchaber, A. 1987 Transitions to turbulence in helium gas. *Phys. Rev.* A **36**, 5870–5873.

Howard, L. N. 1966 Convection at high Rayleigh numbers. *Proc. 11th Intl Congress Appl. Mech.*, pp. 1109–1115.

Jakob, M. 1946 Free heat convection through enclosed plane gas layers. *Trans. ASME* **68**, 189–194.

Kraichnan, R. H. 1962 Turbulent thermal convection at arbitrary Prandtl numbers. *Phys. Fluids* **5**, 1374–1389.

Liu, Y. & Ecke, R. E. 1997 Heat transport scaling in turbulent Rayleigh–Bénard convection: effects of rotation and Prandtl number. *Phys. Rev. Lett.* **79**, 2257–2260.

Malkus, W. V. R. 1954 The heat transport and spectrum of thermal turbulence. *Proc. R. Soc. Lond.* A **225**, 196–212.

Niemela, J. J., Skrbek, L. & Donnelly, R. J. 2000 Turbulent convection at very high Rayleigh numbers. *Nature* **404**, 837–840.

Raithby, G. D. & Hollands, K. G. T. 1985 Natural convection. In *Handbook of Heat Transfer Fundamentals*, 2nd edn. (ed. W. M. Rohsenow, J. P. Harnett & G. N. Ganic). McGraw-Hill.

Wu, X. Z. & Libchaber, A. 1992 Scaling relations in thermal turbulence: the aspect-ratio dependence. *Phys. Rev.* A **45**, 842–845.

Xu, X., Bajaj, K. M. S. & Ahlers, G. 2000 Heat transport in turbulent Rayleigh–Bénard convection. *Phys. Rev. Lett.* **84**, 4357–4360.